



# Synthesis of 3D graphite oxide-exfoliated carbon nanotube carbon composite and its application as catalyst support for fuel cells

Hailin Wang<sup>a</sup>, Bhalchandra A. Kakade<sup>a,c</sup>, Takanori Tamaki<sup>a,b</sup>, Takeo Yamaguchi<sup>a,b,\*</sup>

<sup>a</sup>Chemical Resources Laboratory, Tokyo Institute of Technology, R1-17, 4259 Nagatsuta, Midori-ku, Yokohama 226-8503, Japan

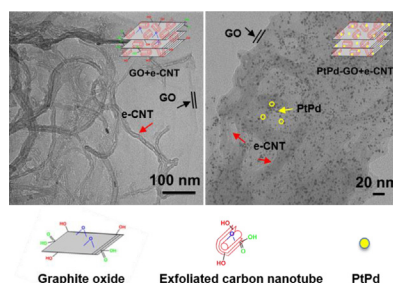
<sup>b</sup>KAST, Kanagawa Academy of Science and Technology, Japan

<sup>c</sup>SRM Research Institute, SRM University, Kattankulathur, Chennai 603 203, India

## HIGHLIGHTS

- e-CNT was firstly applied as effective carbon spacer to prevent graphene from restacking.
- Thermally reduced GO + e-CNT shows enhanced surface area and interlayer distance compared to thermally reduced GO.
- The unique 3D morphology was confirmed by TEM and cross-section HR-TEM.
- GO + e-CNT supported PtPd shows homogenous particle distribution with enlarged ECSA value and mass activity toward MOR.

## GRAPHICAL ABSTRACT



## ARTICLE INFO

### Article history:

Received 8 November 2013

Received in revised form

21 February 2014

Accepted 8 March 2014

Available online 15 March 2014

### Keywords:

Graphite oxide

Exfoliated carbon nanotube

Catalyst support

Methanol oxidation reaction

Fuel cells

## ABSTRACT

The restacking of graphene or reduced graphite oxide (r-GO) is commonly regarded as a severe obstacle for potential applications. We propose the application of exfoliated carbon nanotube (e-CNT) as an effective carbon spacer for fabricating a sandwich-like three-dimensional (3D) carbon composite with GO. The 3D carbon combination of GO + e-CNT is successfully prepared via homogeneously mixing of GO and e-CNT in an aqueous dispersion in which carbon spacers are homogeneously intercalated with graphene layers. With the addition of a carbon spacer, the BET surface area of 3D carbon ( $51.6 \text{ m}^2 \text{ g}^{-1}$ ) is enhanced by a factor of three compared with r-GO ( $17.2 \text{ m}^2 \text{ g}^{-1}$ ) after thermal reduction. In addition, the 3D GO + e-CNT supported PtPd catalyst (PtPd-GO + e-CNT) shows homogenous distribution of PtPd nanoparticles of  $3.9 \pm 0.6 \text{ nm}$  in size, with an enlarged electrochemical active surface area (ECSA) value of  $164 \text{ m}^2 \text{ g}^{-1}$  and a mass activity of  $690 \text{ mA mg}^{-1}$  toward the methanol oxidation reaction (MOR), which is the typical anode reaction for direct methanol fuel cells (DMFC).

© 2014 Elsevier B.V. All rights reserved.

## 1. Introduction

Nanostructured carbon is a low-cost and versatile functional material that shows great potential in energy storage, [1] solar cells, [2] electronic devices, [3] sensors, [4] as well as fuel cells [5]. The maximum utilization of surface of noble catalyst materials to reduce the high cost of fuel cells, nanostructured carbon materials, such as activated carbon and carbon nanotubes, have been widely

\* Corresponding author. Chemical Resources Laboratory, Tokyo Institute of Technology, R1-17, 4259 Nagatsuta, Midori-ku, Yokohama 226-8503, Japan. Tel.: +81 45 924 5253; fax: +81 45 924 5254.

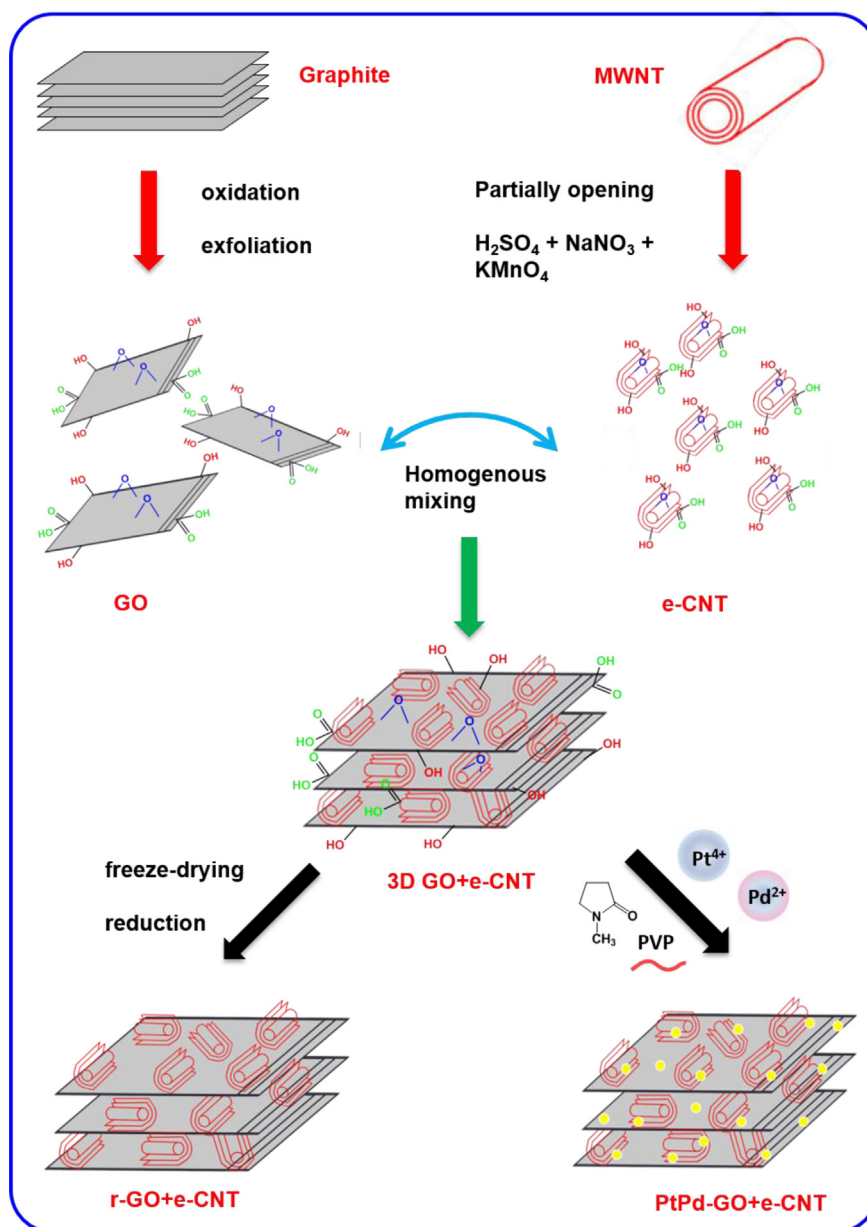
E-mail address: [yamag@res.titech.ac.jp](mailto:yamag@res.titech.ac.jp) (T. Yamaguchi).

used as catalyst-support materials due to their large surface area, high electron conductivity, and relatively good stability in fuel cell working conditions [6,7]. To date, graphene, a two-dimensional (2D) one-atom-thick carbon layer with an unusual quantum Hall effect, large surface area, high electric conductivity, and low manufacturing cost [8–12] is drawing much attention for applications such as novel electronic devices, [13,14] chemical sensors, [15,16] and energy conversion [17–24].

However, 2D graphene always tend to stack together because of the strong  $\pi$ – $\pi$  interaction, and this could significantly suppress various properties of graphene. In particular, when applying graphene as catalyst support for polymer electrolyte fuel cells (PEFCs), this restacking could result in the loss of effective supporting area and electrolyte accessibility, leading to the lower utilization of noble metal nanoparticles [25]. To prevent the restacking of graphene layers, one promising approach is to incorporate carbon spacers with graphite oxide (GO), since GO with hydrophilic

functional groups can be easily exfoliated in aqueous dispersion to facilitate 3D network of carbon using spacers. Recently, considerable efforts have been invested in preventing this restacking of neighboring carbon layers, including compositing GO with carbon spacers, such as functionalized carbon nanotubes (f-CNTs) [26] or carbon black (CB) [27,28]. Nevertheless, the interactions between the graphene layers and the carbon spacers were still ineffective, perhaps because of the converse properties of GO (strongly hydrophilic) and carbon spacers (weakly hydrophilic or hydrophobic). To effectively prevent the restacking of graphene layers, it is necessary to search for alternative carbon spacers.

Exfoliated carbon nanotube (e-CNT) can be regarded as a highly hydrophilic, chemically unzipped multiwalled carbon nanotube (MWNT), as shown in Scheme 1a. The e-CNT prepared via the modified Hummers method shows both entangled graphene nanoribbon oxide layers and residual inner carbon tubes [29,30]. This unique property and structure make it a promising carbon



**Scheme 1.** Schematic images representing (a) preparation of e-CNT, (b) self-assembling of 3D carbon composite, (c) study of the carbon spacer effect by thermal reduction, and (d) preparation of the 3D catalyst.

spacer for preventing restacking of graphene layers. First, these hydrophilic oxidized layers in e-CNT could easily be incorporated with GO into a three-dimensional (3D) sandwich-like network driven initially by homogeneously mixing in water dispersion due to the presence of various hydrophilic moieties like epoxide, hydroxyl and carboxyl etc., and the electrostatic repulsion force between GO and e-CNT can be neglected due to the mismatched size [31]. Second, the residual tube inserted among the graphene layers could hold the carbon layers from restacking, which could also increase ion accessibility to the interlayers. Furthermore, the residual tube could also effectively increase the surface area by forming a 3D network. In this study, first the 3D carbon composite GO + e-CNT was obtained in a homogenous aqueous dispersion of GO and e-CNT mixture (Scheme 1b). Then, to check the carbon spacer effect in preventing the restacking of graphene, the 3D carbon composite was thermally reduced (named r-GO + e-CNT, Scheme 1c). Our results showed that the 3D morphology was successfully fabricated with expanded interlayer distance and increased surface area, which holds promising potential as electrode materials for supercapacitors or catalyst support for fuel cells. On the other hand, Pt-based nanocrystals have so far been regarded as the most effective catalysts for accelerating electrode reactions of PEFC [32]. In our group, monodispersed and shape-controlled PtPd nanoparticles with enhanced catalytic activities were prepared via the simple one-pot method [33,34]. Nevertheless, increasing the utilization of precious metal catalysts by decorating active nanocrystals on nanostructured carbon support materials via a simple approach [35–37] is still challenging. PtPd nanocrystals were fabricated with 3D carbon composite using a facile chemical coreduction method named PtPd-GO + e-CNT (shown schematically in Scheme 1d).

In the present work, e-CNT was first applied as a carbon spacer because of its unique structure and properties for fabricating the sandwich-like 3D carbon composite GO + e-CNT. Moreover, the carbon spacer effect was studied after reducing mixtures of varying ratios of GO and e-CNTs by the simple thermal method. Furthermore, the 3D carbon composite-supported PtPd electrocatalyst was also prepared via the facile coreduction method. The catalytic performance towards a methanol oxidation reaction (MOR), which is a typical anode reaction for DMFCs was also studied. 3D catalysts showed a dramatic increase in the electrochemically active surface area (ECSA) (PtPd-GO + e-CNT,  $164 \text{ m}^2 \text{ g}_{\text{Pt}}^{-1}$ ) and mass-specific activities ( $I_m$ ) (PtPd-GO + e-CNT,  $690 \text{ mA mg}^{-1}$ ) toward MOR, demonstrating that 3D carbon composite is a promising catalyst support for fuel cell applications.

## 2. Experimental

### 2.1. Materials

Hexachloroplatinic acid ( $\text{H}_2\text{PtCl}_6 \cdot 6\text{H}_2\text{O}$ ), graphite powder, 30% hydrogen peroxide ( $\text{H}_2\text{O}_2$ ), potassium permanganate ( $\text{KMnO}_4$ ),  $\text{H}_2\text{SO}_4$  (98%),  $\text{HClO}_4$  and solvents such as N-methyl 2-pyrrolidone (NMP), ethanol, methanol, and acetone were purchased from Wako Pure Chemicals Industries, Japan. MWNTs with a diameter of 8–10 nm were purchased from Chemapol Industries, India. Palladium (II) chloride ( $\text{PdCl}_2$ ), PVP, and MW 55000 were purchased from Aldrich chemicals. Commercial Pt–C (19.3%, TEC10E20E) catalyst was purchased from Tanaka Kikinzoku Kogyo, Tokyo, Japan (TKK). Millipore water (18 M $\Omega$ ) Millipore water (18 M $\Omega$ ) was used throughout for all methanol oxidation reaction measurements.

### 2.2. Preparation of GO and e-CNT

Graphite oxide was synthesized using the Hummers and Offeman method [38]. Briefly, 2 g graphite powder and 1 g  $\text{NaNO}_3$  were

mixed with 46 mL of concentrated  $\text{H}_2\text{SO}_4$ . Next, 6 g of  $\text{KMnO}_4$  was added under ice bath to prevent the temperature from exceeding 20 °C, after which the mixture was stirred and held at 35 °C for 30 min. Then, 92 mL of deionized water was slowly added into the system. After stirring for 15 min, 80 mL of warm water was added. To reduce excess  $\text{KMnO}_4$ , a proper amount of 3%  $\text{H}_2\text{O}_2$  aqueous solution was dropped into the mixture until no bubbles were observed. The mixture was then centrifuged and treated by dialysis to remove the residual impurities. Finally, the product was separated by freeze-drying and e-CNT was synthesized by oxidizing 1 g of MWNT following the same Hummers and Offeman method.

### 2.3. Preparation of GO + e-CNT and r-GO + e-CNT

50 mg of GO and 50 mg of e-CNT were dispersed into 100 mL of deionized water. The dispersion was stirred for 10 min and further treated in ultrasonic bath for 30 min. After that, the dispersion was mixed by a homogenizer probe for 30 min to facilitate the self-assembling process. Then 3D carbon composite GO + e-CNT was separated by freeze-drying. To prepare r-GO + e-CNT, 100 mg of GO + e-CNT was placed in a quartz boat and inserted into the tube furnace. After flowing Ar for 5 min, the sample was heated under the same atmosphere at 300 °C for 3 h. To compare the carbon spacer effect, GO and e-CNT were also thermally reduced using the same conditions, named r-GO and r-e-CNT, respectively.

### 2.4. Decorating PtPd nanocrystals on various carbon substrates

40 mg of GO + e-CNT was redispersed into 40 mL  $\text{H}_2\text{O}$  to obtain  $1 \text{ mg mL}^{-1}$  homogenous dispersion. Next, 3.6 mL of (25 mmol)  $\text{H}_2\text{PtCl}_6$  solution and 0.9 mL (25 mmol) of  $\text{PdCl}_2$  solution were added to the dispersion. After 30 min ultrasonication, 10 mg of PVP and 40 mL NMP were added in the flask. After heating the mixture at 150 °C for 5 h, the product was washed with excess acetone and separated by centrifugation, named PtPd-GO + e-CNT. The actual metal loading was determined by inductively coupled plasma-atomic emission spectroscopy (ICP-AES) measurements. PtPd supported on GO and e-CNT with the same compositions and metal loadings has also been prepared by a similar method for comparison of their methanol electrooxidation.

### 2.5. Characterization

The composition was analyzed using the ICP-AES technique with an ICPS-8100, (Shimadzu) direct current plasma-atomic emission spectrometer. The Brunauer–Emmett–Teller (BET) surface area was measured by BELSORP-mini II (BEL Japan, Inc.) using  $\text{N}_2$  as the adsorption gas. Transmission electron microscopy (TEM) was performed with a Hitachi H-7000 apparatus operating at 100 kV with a resolution better than 3–4 nm to obtain the particle size and its distribution. A drop of the suspension was cast on lacy carbon film-coated Cu microgrids. After drying at room temperature, these grids were then used for structural investigation. High resolution TEM (HR-TEM) was performed on a Hitachi H-9000UHR III at 300 kV. For observation, the 3D carbon composite was first sandwiched with resins and then cut vertically to the carbon plane. X-ray powder diffraction (XRD) was used to measure the phase and size of the nanocrystals at  $2\theta$  angles between 2 and 90° with a scan rate of 5°/min on a RINT 2100 diffractometer (Rigaku Co. Ltd, Japan) using Cu K $\alpha$  radiation ( $\lambda = 1.5418 \text{ \AA}$ , 40 kV, 40 mA). The Fourier transform infrared (FTIR) spectra of GO + e-CNT and r-GO + e-CNT were measured with an FT/IR-6200 spectrophotometer (JASCO Co. Ltd). Wafers of KBr containing a small amount of sample were used to obtain the absorption FTIR spectra in the range of 4000–400  $\text{cm}^{-1}$ . Thermogravimetric analysis (TGA) was performed on a

PerkinElmer Pyris 1 TGA; 4–6 mg of sample was weighed and heated in a Pt pan under dry  $O_2$  atmosphere at a rate of  $10^\circ C\ min^{-1}$ . The Raman spectrum was obtained with an NRS-2100 (JASCO), using a 1 W Ar ion laser. XPS analysis for all the catalysts performed with a Quantera SXM from ULVAC-PHI, Inc., Japan. The X-ray source was monochromatic and focused (spot diameter of  $100\ \mu m$ ) Al  $K\alpha$  radiation, operated at 25 W and 15 kV.

## 2.6. Electrochemical measurements

The glassy carbon (GC) electrode surface (geometric area:  $0.196\ cm^2$ ) was first polished with  $0.05\ \mu m$  alumina slurry, followed by careful rinsing and ultrasonication in deionized water for 3 min. The geometric area of the GC electrode provides a measure of the loading of catalyst on the electrode surface used for the voltammetric characterization. The electrode was coated with the catalyst layer using a modified method from a previous report [39]. Briefly, a typical suspension of the catalyst was prepared by suspending 10 mg of catalysts in 10 mL of 24% isopropyl alcohol (IPA) solution and 40  $\mu L$  of Nafion (5 wt%, Aldrich). Then, 10  $\mu L$  of this catalyst ink was transferred to the surface of the polished and cleaned GC electrode surface. The electrode was dried overnight at room temperature under ethanol atmosphere for slow-rate evaporation. This catalyst-loaded working electrode was then electrochemically cleaned by cycling between 0.06 V and 1.2 V vs RHE in  $N_2$ -saturated 0.1 M  $HClO_4$  solution and the ECSA was determined under similar conditions prior to adding methanol. All potentials mentioned throughout the discussion are referred against RHE. A Pt wire was used as the counter electrode. The hydrogen adsorption/desorption

electric charges calculated from the CV graphs were used to estimate the ECSA of the catalysts. Methanol electrooxidation was studied by adding an appropriate amount of methanol in 0.1 M  $HClO_4$  under  $N_2$  atmosphere solution and voltammograms were recorded.

## 3. Results and discussion

### 3.1. 3D carbon composite

The TEM image in Fig. 1a shows the typical TEM image of GO containing large crystalline graphene oxide layers with folded and wrinkled edges. The inset figure shows the  $0.05\ mg\ mL^{-1}$  aqueous dispersion of GO that was kept for 3 weeks. Because of the high density of hydrophilic functional groups, GO can be easily dispersed in water to yield stable dispersions, and this property could be used for preparation of graphene or composite materials [40]. Fig. 1b shows the unique morphology of e-CNT, revealing partial unzipping of the outer walls of pristine MWNTs. Some of the regions are damaged and become blurry with open parts extending irregularly into various directions because of the high density of functional groups. In addition, unopened residual tubes with a central hollow structure can still be observed, perhaps because of the incomplete oxidation. Similar to GO, e-CNT also possesses excess hydrophilic groups resulting in the formation of stable aqueous dispersion, as shown in the inset photograph of Fig. 1b. The good hydrophilic properties facilitate easy preparation of the 3D carbon composite GO + e-CNT from GO and e-CNT in aqueous solution. The following process is considered for the 3D formation: due the presence of

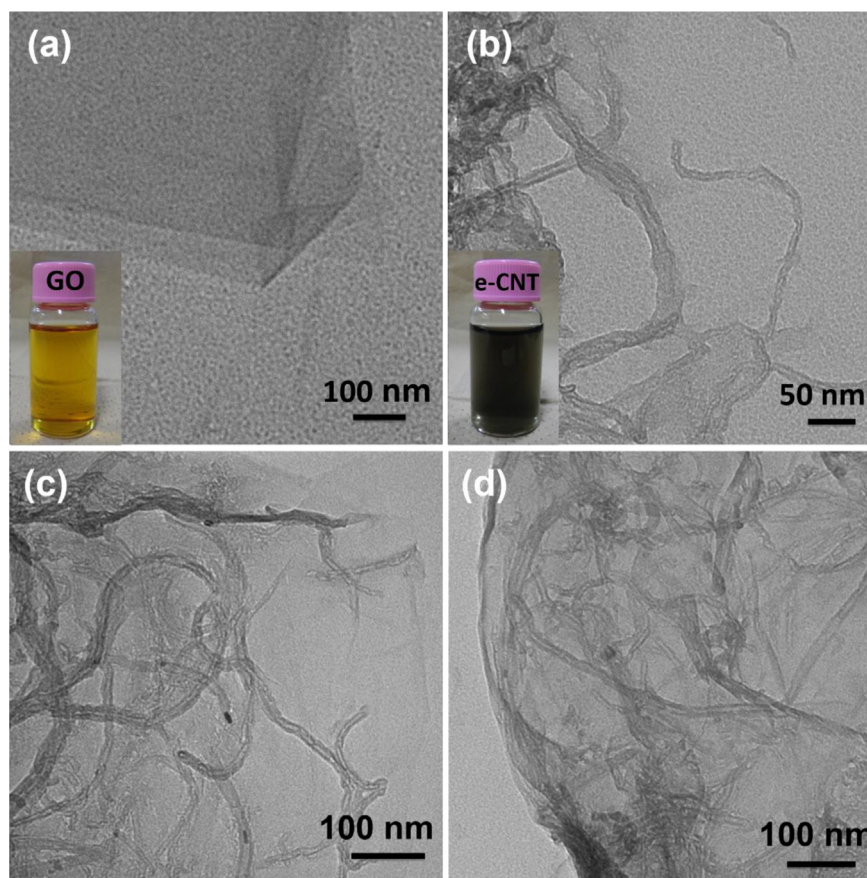


**Fig. 1.** TEM images of (a) GO, (b) e-CNT, (c) the 3D carbon composite GO + e-CNT, and (d) thermally reduced 3D carbon composite (r-GO + e-CNT); the insert photographs show the  $0.05\ mg\ mL^{-1}$  water dispersion of GO and e-CNT, respectively.



high density of functional groups, GO and e-CNT can be easily dispersed into water to form homogenous dispersion. After freeze drying the mixture, restacking of exfoliated GO in presence of e-CNTs occurs among free graphitic layers of e-CNTs (due to exfoliation) into GO layers. The TEM image in Fig. 1c reveals the top view of the 3D morphology, in which the tubular-like e-CNT can be clearly observed being randomly distributed among the large graphene oxide layers. Apart from the residue tubes, the broken layers of e-CNT behave like small graphene oxide layers that have overlapped above the large carbon lattices of GO or merged into the gaps between different graphene oxide layers leading to a well-interacted 3D network. Fig. 1d shows the morphology of r-GO + e-CNT after reduction, and the interaction between e-CNT and GO can also be clearly observed, indicating that the 3D morphology is maintained during the freeze-drying and thermal reduction process. In addition, folded and wrinkled edges as well as defects are formed as a result of the loss of functional groups.

The irreversible restacking of GO after losing functional groups has been well reported, thus leading to less utilization of the interlayer spaces despite regaining the good electron conductivity. In this study, we suggest that 3D carbon is a promising design that could harvest more surface area by intercalating e-CNTs into the carbon lattices. First, the reduction of 3D carbon is confirmed by the Raman spectrum in Fig. 2a. Both GO + e-CNT and r-GO + e-CNT show one typical G-peak  $\sim 1600\text{ cm}^{-1}$ , corresponding to the  $E_{2g}$  vibrational mode, and one D-peak  $\sim 1350\text{ cm}^{-1}$ , revealing a disordered structure and defects [41,42]. After reduction, a red shift of the G-peak of r-GO + e-CNT ( $1602\text{ cm}^{-1}$ ) to GO + e-CNT ( $1608\text{ cm}^{-1}$ ) is observed. This result demonstrates that reduction of 3D carbon is performed as the G-peak shifted nearer to the pristine graphite position [43,44]. Reduction is further confirmed by the FTIR spectrum (Fig. 2b). r-GO + e-CNT shows the intensity suppression of all the absorption peaks between  $1000\text{ cm}^{-1}$  and  $2000\text{ cm}^{-1}$ , indicating the loss of various functional groups [44]. Due to the effective reduction, r-GO + e-CNT shows 6 orders of magnitude higher conductivity than GO + e-CNT. In addition, the TG curves of GO + e-CNT in Fig. 2c show two major weight losses at around  $200^\circ\text{C}$  and  $450^\circ\text{C}$ , possibly as a result of pyrolysis of the oxygenated functional groups [45]. However, r-GO + e-CNT shows no obvious weight loss before  $450^\circ\text{C}$ , pointing to the absence of the functional groups after heat treatment.

In addition, the structural changes of 3D carbon before and after reduction are studied by XRD. Fig. 3a shows the reflection patterns of various carbons before reduction. The appearance of a new peak at  $11.1^\circ$  in GO indicates the increase of the interlayer distance from  $0.33\text{ nm}$  in graphite powder (Fig. 3c) to  $0.75\text{ nm}$  because of the generation of hydroxyl, epoxy, and carboxyl groups [46]. On the other hand, the XRD pattern of e-CNT shows two broad peaks at  $11.2^\circ$  and  $25.7^\circ$ , attributed to the (001) and (002) planes, respectively. The (002) peak originated from the residual inner nanotubes (Fig. 3d) and the presence of the (001) peak proves the expansion of the interlayer distance as a result of the partial unzipping of the carbon nanotube [30]. For GO + e-CNT, it shows a predominant (001) peak attributed to the overlapping of graphene oxide layers between GO and e-CNT as well as a small (002) peak belonging to the residual tubular structure of e-CNT. As shown in Fig. 3b, the (001) peak at  $11^\circ$  has disappeared for all carbons after thermal reduction, which agrees well with the results in Fig. 2. In addition, r-GO + e-CNT shows one evident broad peak at  $26^\circ$ , and this is attributed to (002) peaks of the tubular structure of e-CNT, as can be confirmed from the XRD patterns of r-e-CNT (Fig. 3b) and MWNT (Fig. 3d). Apart from that, the shoulder diffraction peak at  $20^\circ$  is the (002) peak originated from graphene layers. Compare to the diffraction peak of r-GO (Fig. 3b) at  $22^\circ$ , the (002) peak of r-GO + e-CNT at  $20^\circ$  showed a negative shift, indicating that the interlayer

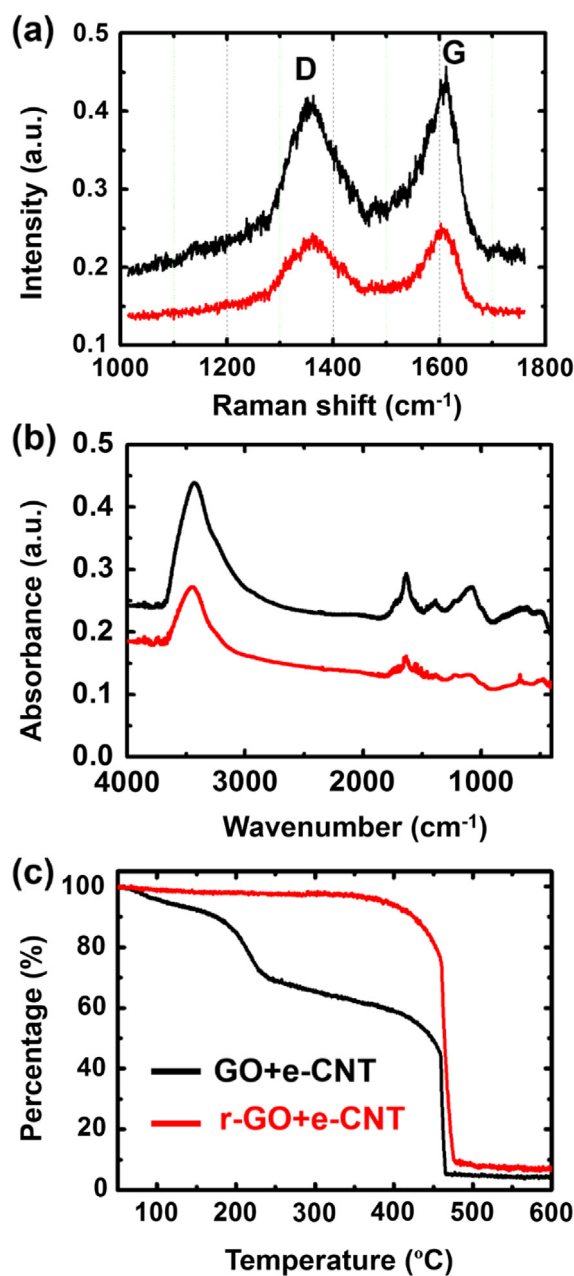
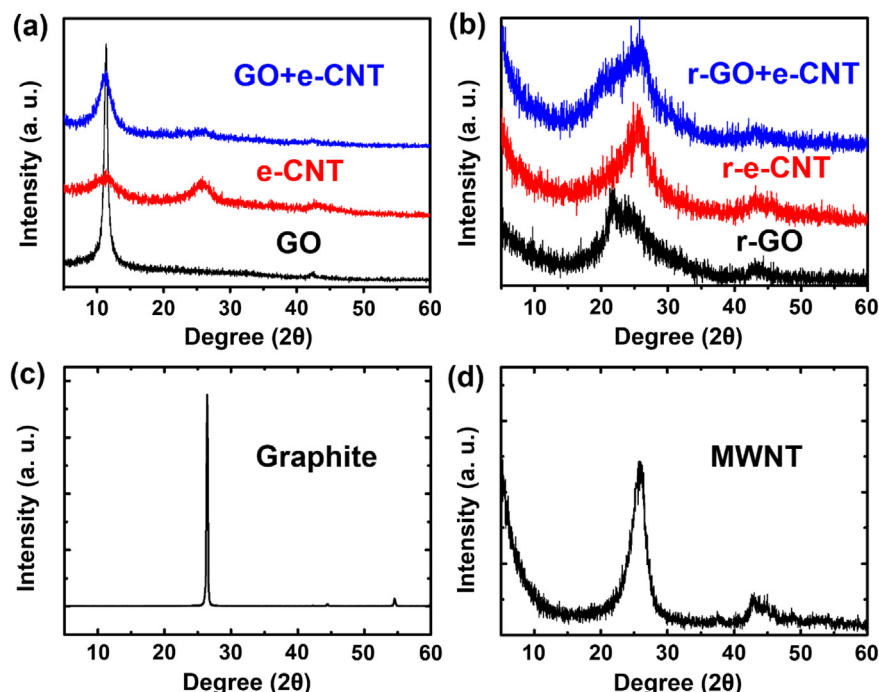


Fig. 2. Comparative study of the 3D carbon composite before and after reduction: (a) Raman spectra, (b) FTIR spectrum, (c) TG curves of GO + e-CNT (i) and r-GO + e-CNT (ii).

distance between the graphene layers has been successfully enlarged in the 3D architecture.

The carbon spacer effect is further confirmed through the cross-section view using HR-TEM. Fig. 4a reveals the cross-section view of 3D r-GO + e-CNT at low magnification. It shows a large carbon flake with a thickness ranging from 11 to 35 nm, indicating the partial expansion of graphene layers. In addition to the homogenous interactions between GO and e-CNT, some aggregation of e-CNTs can be observed in a certain area. This phenomenon can be attributed to the favorable interactions at regions with more functional groups or defects. Fig. 4b shows the enlarged view of a selected area, showing the interaction between graphene layers and carbon spacers. To better understand the effect, the border between the two carbon materials in this same area has been marked out in



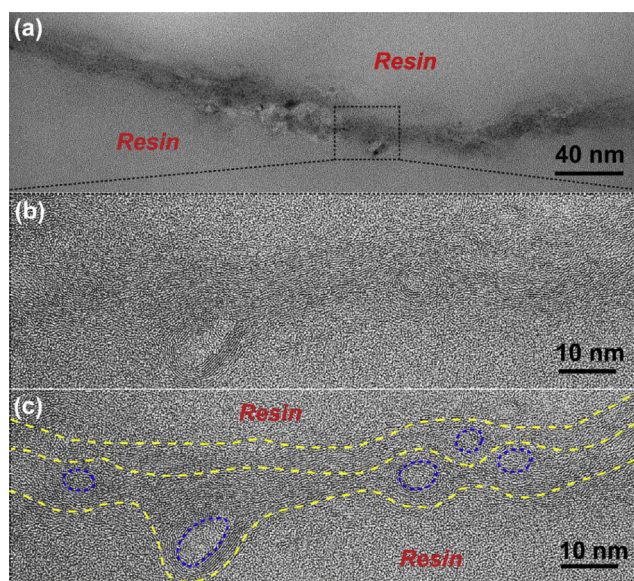
**Fig. 3.** XRD patterns of: (a) GO, e-CNT, and GO + e-CNT; (b) r-GO, r-e-CNT, and r-GO + e-CNT; (c) pristine graphite powder; and (d) untreated multi-walled carbon nanotube (MWNT).

**Fig. 4c.** Several lines belonging to the graphene layers can be clearly observed, among which a few groups of concentric circles are inserted as marks by the dashed cycles. In addition, the diameter of each cycle is around 5 nm, with one exception, which is probably cut inclined vertical to the central axis. In addition, the diameter of the carbon spacer is smaller than the pristine MWNT, which is caused by the partial exfoliation of the outer layers. This is strong evidence that e-CNT has been successfully inserted among the graphene layers. Apart from the HR-TEM image, BET analysis also

demonstrates that the 3D carbon composite shows a significant increase in surface area, i.e.  $51.6 \text{ m}^2 \text{ g}^{-1}$ , three times higher than r-GO ( $17.2 \text{ m}^2 \text{ g}^{-1}$ ) and 1.4 times larger than r-e-CNT ( $36.9 \text{ m}^2 \text{ g}^{-1}$ ), as shown in Table 1. These results demonstrate that e-CNT can be easily mixed with graphene layers and homogeneously inserted into the graphene layers or merged onto the outer layer and edges. This unique 3D structure is interesting as catalyst support. The abundant and well-distributed functional groups, edges, and defects before reduction can provide sufficient arching points for supporting metal nanocrystals. More importantly, the 3D architecture can be maintained and the restacking of graphene layers can be prevented by carbon spacers that ensure that a more effective surface area could be harvested for distributing nanoparticles. A previous study intercalated graphene layers with conducting polyaniline nanofibers [47] and reported 3D composite materials that showed an obvious increased surface area and enhanced supercapacitance of the restacked graphene layers. Hence, our 3D carbon composite is also expected to be a promising material for energy storage applications.

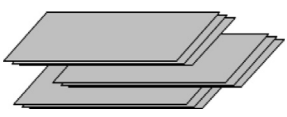
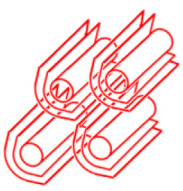
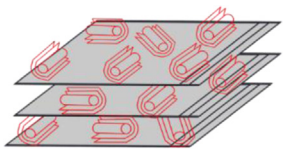
### 3.2. 3D carbon-supported PtPd catalyst

It is practically challenging to achieve a homogeneous distribution of metal nanoparticles on carbon support materials. The chemical coreduction method, in which metal ions are reduced after interacting with functional groups or defects on a carbon substrate, is one of the well-known methods, in particular for graphene-based carbon candidates [48–52]. In this study, PtPd decorated on 3D carbon composite, named PtPd-GO + e-CNT is conducted by mixing metal ions with negatively charged 3D carbon composite GO + e-CNT to form metal-carbon complex. After adding the reducing reagent, the complex will be reduced leading to formation of PtPd nanoparticles with concomitant removal of surface functional groups. Eventually, this will affect in regaining the electronic structure of carbon. For comparison, only GO and e-CNT



**Fig. 4.** Cross-sectional HR-TEM images of r-GO + e-CNT (a) at low magnification, (b) at high magnification, and (c) the same area with indicating lines between the boundaries.

**Table 1**  
BET surface area values of various carbon materials after reduction.

Carbon materials	Schematic image	BET surface area ( $\text{m}^2 \text{g}^{-1}$ )
r-GO		17.2
r-e-CNT		36.9
r-GO + e-CNT		51.6

supported PtPd electrocatalysts are also prepared by the similar procedure, named PtPd-GO and PtPd-e-CNT, respectively. The XRD patterns demonstrate that all the carbon diffraction peaks shifted back to the (002) region ( $\sim 26^\circ$ ), indicating that all the carbon-supported materials are effectively reduced. [53]. In addition, the PtPd nanocrystal can be indexed into the (111), (200), (220), and (311) planes of a face-centered cubic lattice, as shown in Fig. 5. In Fig. 6, the C1s XPS spectra of all the catalysts, show similar peak to the spectra of carbon supported electrocatalyst [21,49], indicating that the oxygenated functional groups on the carbon substrate have been effectively removed. In addition, the appearance of significant Pt4f (70.6 eV and 74.0 eV respectively for Pt4f<sub>7/2</sub> and Pt4f<sub>5/2</sub>) and Pd3d (335.0 eV and 340.3 eV respectively for Pd3d<sub>5/2</sub> and Pd3d<sub>3/2</sub>) signals indicate the presence of Pt and Pd. Furthermore, the Pt4f

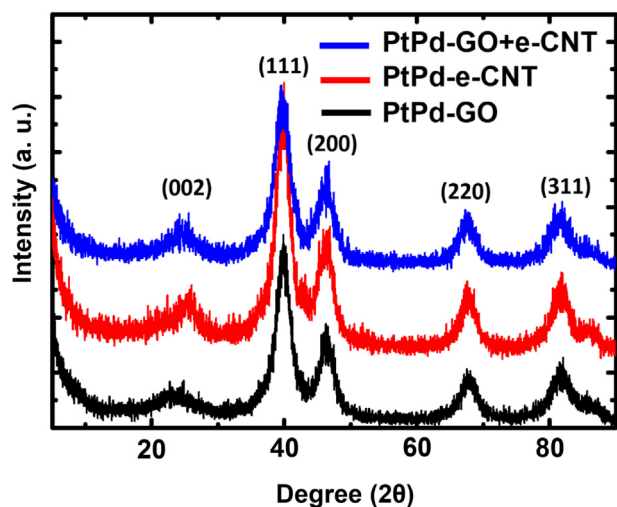


**Fig. 5.** Comparison of XRD patterns of PtPd-GO (a), PtPd-e-CNT (b), and PtPd-GO + e-CNT (c).

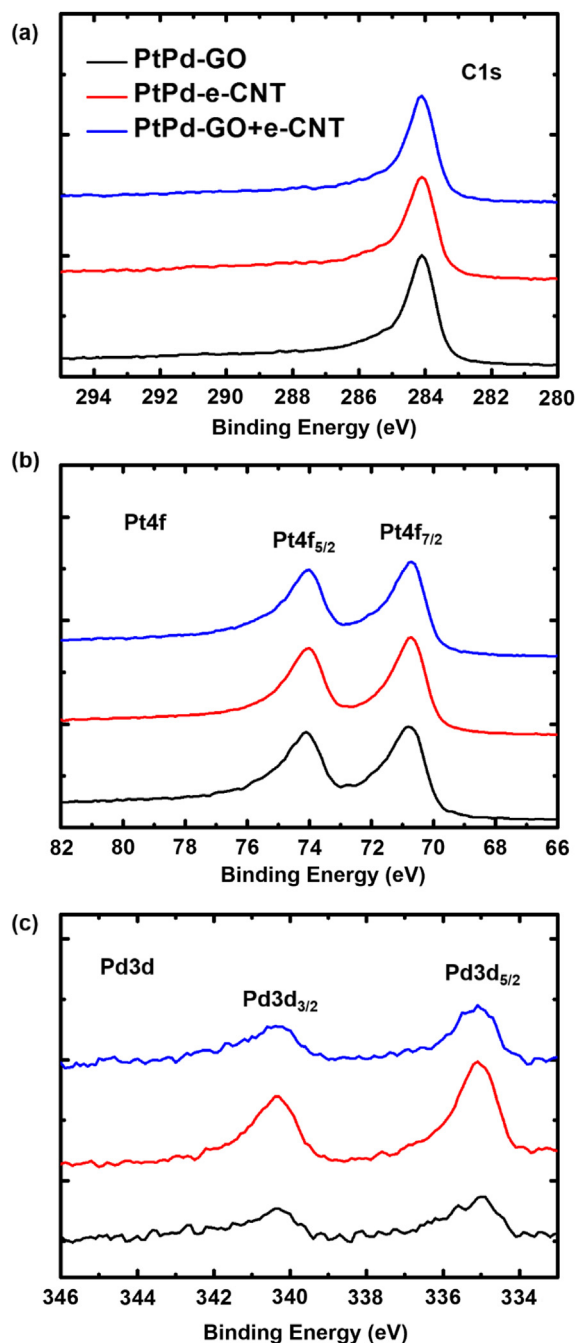


**Fig. 6.** XPS spectra of PtPd-GO (dashed line), PtPd-e-CNT (dashed-dotted line) and PtPd-GO + e-CNT (solid line) (a) C1s binding region, (b) Pt4f binding region and (c) Pd3d binding region.

signals (Fig. 7) can be deconvoluted into three pairs of doublets, corresponding to the Pt(0), Pt(II) and Pt(IV) states, respectively. The relative intensities of the Pt(0) to the oxidized states for all the catalysts are PtPd-GO (76%), PtPd-e-CNT(84%), and PtPd-GO + e-CNT(77%). All the catalysts show similar high amount of metallic Pt ( $>70\%$ ) due to the sufficient reduction.

The unique morphology of the 3D catalyst is further confirmed by TEM images. PtPd-GO (Fig. 8a) reveals large and uniform crystalline graphene sheets with heterogeneously distributed PtPd nanoparticles of average size of  $3.5 \pm 1.1$  nm (average diameter of 50 randomly taken particles). PtPd-e-CNT shows the morphology of



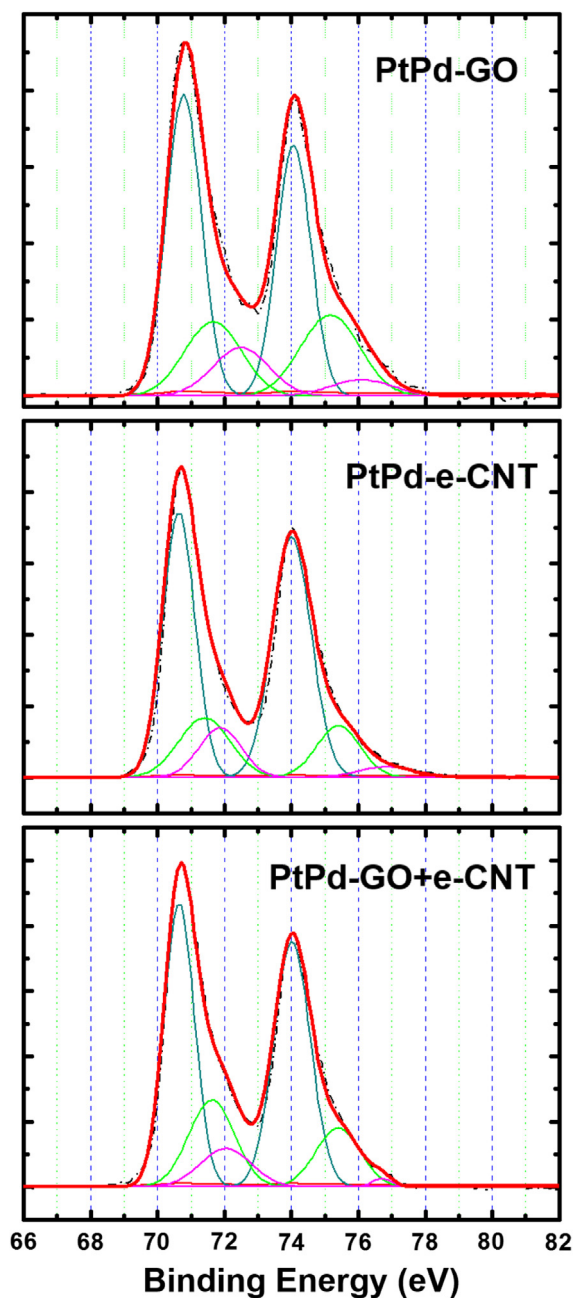


Fig. 7. Pt4f XPS spectra of PtPd-GO, PtPd-e-CNT and PtPd-GO + e-CNT.

e-CNT (Fig. 8b) with both residual tubes and partially open parts, among which the  $5.3 \pm 0.5$  nm PtPd nanoparticles are uniformly supported. The 3D catalyst PtPd-GO + e-CNT (Fig. 8c) illustrates that PtPd nanoparticles are homogeneously distributed among the 3D network with average size of  $3.9 \pm 0.6$  nm. Because of the interaction between GO and e-CNT, the 3D carbon substrate provides more available interacting sites and supporting area for the metal ions and thus facilitates the nucleation formation process.

The electrochemical activity of the 3D catalyst is tested in a three-electrode system. All the catalysts show a distinct hydrogen adsorption/desorption region, a double layer region, and a surface oxide formation/reduction region (Fig. 9a). Compared with PtPd-GO and PtPd-e-CNT, the 3D catalyst shows the highest adsorption/desorption current, indicating well-exposed catalytic sites for the surface redox process. The ECSA values are calculated from the

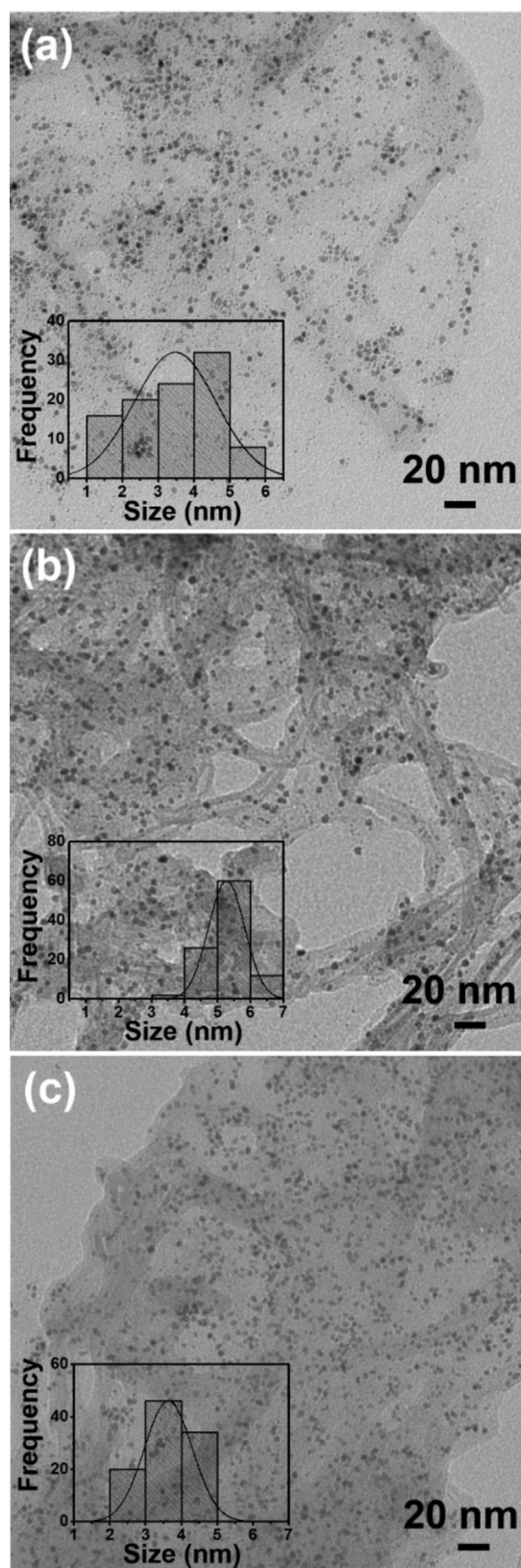
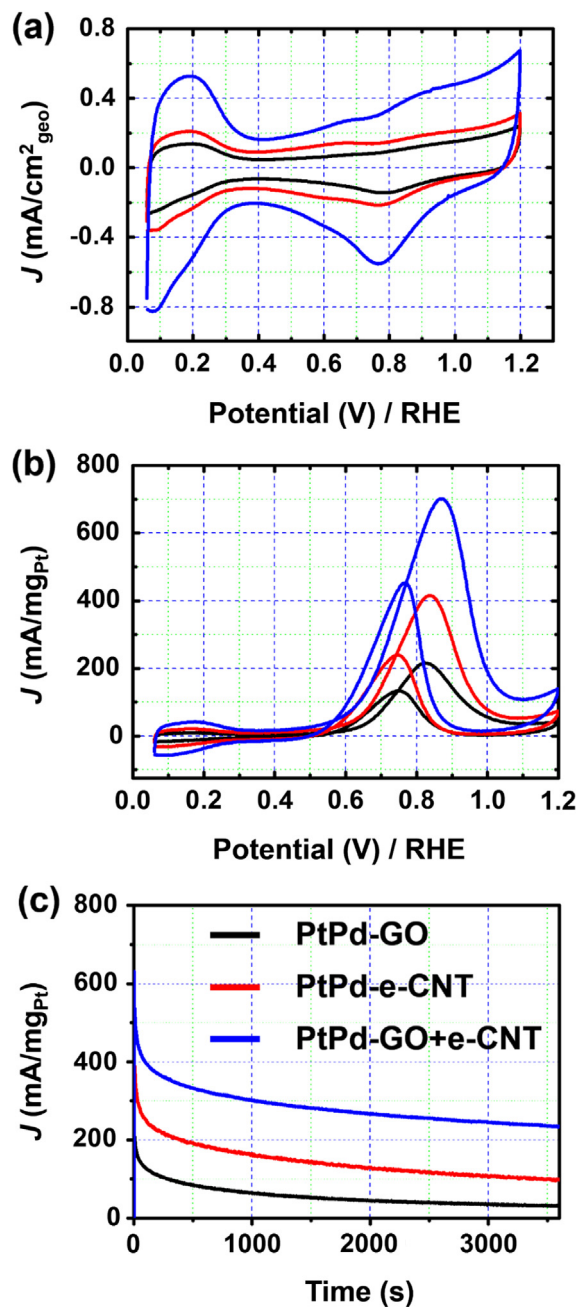


Fig. 8. TEM images and size distributions of (a) PtPd-GO, (b) PtPd-e-CNT, and (c) PtPd-GO + e-CNT.





**Fig. 9.** (a) CV curves in 0.1 M HClO<sub>4</sub> under N<sub>2</sub> atmosphere recorded at the scan speed of 20 mV s<sup>-1</sup>, (b) CVs for MOR in 0.1 M HClO<sub>4</sub> and 0.1 M methanol under N<sub>2</sub> atmosphere, (c) current stability at 0.8 V by chronoamperometry in 0.1 M HClO<sub>4</sub> and 0.1 M methanol under N<sub>2</sub> atmosphere of PtPd-GO (dashed line), PtPd-e-CNT (dashed-dotted line), and PtPd-GO + e-CNT (solid line).

hydrogen adsorption–desorption charge ( $Q_H$ ) after subtraction of the non-Faradic currents. As listed in Table 2, PtPd-GO + e-CNT shows ECSA values of 164 m<sup>2</sup> g<sup>-1</sup>, which is 3.3 times higher than that of PtPd-GO (50 m<sup>2</sup> g<sup>-1</sup>), and 2.9 times higher than PtPd-e-CNT

(56 m<sup>2</sup> g<sup>-1</sup>), respectively. Furthermore, our results also indicate significant enhancement of state-of-the-art works, such as Pt supported on graphene (141.6 m<sup>2</sup> g<sup>-1</sup>), [53] PtPd nanodendrites on graphene nanosheets (81.6 m<sup>2</sup> g<sup>-1</sup>), [18] and Pt on graphene/CNT composite (108 m<sup>2</sup> g<sup>-1</sup>), [25] as well as commercial catalyst TKK Pt–C (81 m<sup>2</sup> g<sup>-1</sup>) (Fig. 10a), indicating 3D carbon is a promising catalyst support for fuel cells. ICP analysis of the Pt/Pd ratios and metal loadings show negligible differences between catalysts; hence, one of the explanations for this unusually large ECSA of the 3D catalysts can be the small particle size effect and homogenous distribution. More importantly, the 3D catalyst also shows enlarged double-layer current, which is mainly attributed to the high surface area and roughness factor of the carbon substrate. At the same potential scan speed, the carbon substrate with a higher double-layer current demonstrates a higher charging between the electrode surface and the electrolyte, which is mainly attributed to the larger surface area of the unique 3D structure.

MOR activities are measured in a 0.1 M HClO<sub>4</sub> solution containing 0.1 M methanol under N<sub>2</sub> atmosphere with scan speed of 20 mV s<sup>-1</sup>. Table 2 and Fig. 9b show clearly that the 3D catalysts in the present case show superior activities toward methanol electrooxidation. Because of the high active surface area, the mass current density of PtPd-GO + e-CNT in the positive direction sweep (690 mA mg<sub>Pt</sub><sup>-1</sup>) is ~3.2 times higher than that of PtPd-GO (214 mA mg<sub>Pt</sub><sup>-1</sup>), and ~1.7 times higher than that of PtPd-e-CNT (415 mA mg<sub>Pt</sub><sup>-1</sup>) as well as ~1.68 times higher than TKK Pt–C (410 mA mg<sub>Pt</sub><sup>-1</sup>) (Fig. 10b). These results indicate the highest utilization of precious metals for promoting the reaction kinetics. Apart from that, another important index of MOR performance is the CO tolerance factor to the carbonaceous species accumulation, by taking the ratio of the forward oxidation current ( $I_f$ ) to the backward current ( $I_b$ ). The results show that the CO tolerance factor for all the catalysts including PtPd-GO + e-CNT, PtPd-GO and PtPd-e-CNT is 1.6. To be noticed that, all these catalysts show higher CO tolerance value (greater than 1) revealing a better oxidation of methanol to carbon dioxide during the positive scan and less accumulation of poisoning species on the catalyst surface. Since the removal of CO is facilitated by adding the second metal Pd, which may act by weakening the Pt–CO bond, and/or by promoting the oxidation of CO to CO<sub>2</sub> via activation of water in an adjacent site to facilitate the formation of the second C–O bond [33]. In addition, the current stability of PtPd-GO + e-CNT is also tested and compared with PtPd-GO and PtPd-e-CNT using single-step chronoamperometry at 0.8 V against RHE. Fig. 9c indicates that when held at the same potential, the current density of all the catalysts drop rapidly at the initial stage, which can be attributed to the generation of poison species such as CO and CHO [54,55]. When reaching the steady state, the 3D catalyst still shows the highest mass activity compared with PtPd-GO and PtPd-e-CNT. This trend also agrees with the cyclic voltammetry and MOR results. Above all, these half-cell results demonstrate 3D carbon a promising supporting material for fuel cells. To improve the utilization of metal catalyst in practical membrane electrode assembly (MEA) fabrication, 3D carbon supported catalyst can be fabricated with size-controlled capping ionomers (~5 nm size) consisting of Zirconium-based nanoparticles and organic proton conductors to form more homogenous three phase boundary [56,57].

**Table 2**  
Summary of catalytic properties of PtPd-GO, PtPd-e-CNT, and PtPd-GO + e-CNT.

Catalysts	Particle size (nm)	Metal loading (wt%)	ECSA (m <sup>2</sup> g <sub>Pt</sub> <sup>-1</sup> )	MOR $I_m$ (mA mg <sub>Pt</sub> <sup>-1</sup> )
PtPd-GO	3.5 ± 1.1	Pt: 18.3, Pd: 4.0	50	214
PtPd-e-CNT	5.3 ± 0.5	Pt: 16.9, Pd: 3.4	56	415
PtPd-GO + e-CNT	3.9 ± 0.6	Pt: 18.6, Pd: 3.7	164	690

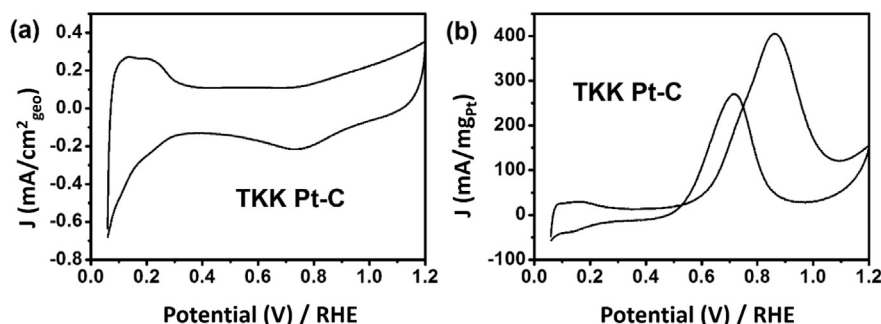


**Fig. 10.** Electrochemical test of commercial catalyst TKK Pt-C (a) CV curve in 0.1 M HClO<sub>4</sub> under N<sub>2</sub> atmosphere recorded at the scan speed of 20 mV s<sup>-1</sup>, (b) CVs for MOR in 0.1 M HClO<sub>4</sub> and 0.1 M methanol under N<sub>2</sub> atmosphere.

#### 4. Conclusions

Exfoliated carbon nanotubes (e-CNTs) with hydrophilic graphene nanoribbon oxide layers and residual tubes were successfully prepared and worked as an effective carbon spacer to intercalate with graphite oxide (GO) forming a sandwich-like 3D carbon composite. The graphene nanoribbon oxide layers in e-CNT induced self-assembling with GO between hydrophilic groups and the residual tubes prevented the restacking of graphene layers when carbon lost functional groups. The 3D carbon composite with increased surface area, enlarged interlayer distance, and arching sites have potential as a promising material for energy storage or catalyst support. In addition, PtPd nanoparticles decorated on 3D carbon composite showed homogeneously distributed  $3.9 \pm 0.6$  nm nanoparticles with an enlarged ECSA value of  $164 \text{ m}^2 \text{ g}^{-1}$  and mass activity of  $690 \text{ mA mg}^{-1}$  toward methanol oxidation, which is superior to GO- or e-CNT-supported PtPd and most state-of-the-art graphene-based electrocatalysts. It was demonstrated that the 3D carbon composite had great potential for improving the utilization of precious metal catalysts for PEMFCs.

#### Acknowledgment

The authors thank for the financial support of KAST project, and H.W. thanks for the financial support of JSPS KAKENHI Grant number 25 5683.

#### References

- [1] C.M. Yang, Y.J. Kim, M. Endo, H. Kanoh, M. Yudasaka, S. Iijima, K. Kaneko, *J. Am. Chem. Soc.* 129 (2006) 20–21.
- [2] A.C. Dillon, *Chem. Rev.* 110 (2010) 6856–6872.
- [3] S. Ravindran, S. Chaudhary, B. Colburn, M. Ozkan, C.S. Ozkan, *Nano Lett.* 3 (2003) 447–453.
- [4] C. Cha, S.R. Shin, N. Annabi, M.R. Dokmeci, A. Khademhosseini, *ACS Nano* 7 (2013) 2891–2897.
- [5] M. Uchida, Y. Fukuoka, Y. Sugawara, N. Eda, A. Ohta, *J. Electrochem. Soc.* 143 (1996) 2245–2252.
- [6] H. Liu, C. Song, L. Zhang, J. Zhang, H. Wang, D.P. Wilkinson, *J. Power Sources* 155 (2006) 95–110.
- [7] S. Zhang, Y. Shao, G. Yin, Y. Lin, *J. Mater. Chem. A* 1 (2013) 4631–4641.
- [8] J.S. Bunch, A.M. van der Zande, S.S. Verbridge, I.W. Frank, D.M. Tanenbaum, J.M. Parpia, H.G. Craighead, P.L. McEuen, *Science* 315 (2007) 490–493.
- [9] A.K. Geim, K.S. Novoselov, *Nat. Mater.* 6 (2007) 183–191.
- [10] V. Singh, D. Joung, L. Zhai, S. Das, S.I. Khondaker, S. Seal, *Prog. Mater. Sci.* 56 (2011) 1178–1271.
- [11] S. Park, R.S. Ruoff, *Nat. Nano* 4 (2009) 217–224.
- [12] K.S. Novoselov, A.K. Geim, S.V. Morozov, D. Jiang, M.I. Katsnelson, I.V. Grigorieva, S.V. Dubonos, A.A. Firsov, *Nature* 438 (2005) 197–200.
- [13] X. Geng, L. Niu, Z. Xing, R. Song, G. Liu, M. Sun, G. Cheng, H. Zhong, Z. Liu, Z. Sun, L. Zhang, H. Xu, L. Lu, L. Liu, *Adv. Mater.* 22 (2010) 638–642.
- [14] J.O. Hwang, D.H. Lee, J.Y. Kim, T.H. Han, B.H. Kim, M. Park, K. No, S.O. Kim, *J. Mater. Chem.* 21 (2011) 3432–3437.
- [15] H. Dong, W. Gao, F. Yan, H. Ji, H. Ju, *Anal. Chem.* 82 (2010) 5511–5517.
- [16] J. Lu, I. Do, L.T. Drzal, R.M. Worden, I. Lee, *ACS Nano* 2 (2008) 1825–1832.
- [17] X.-C. Dong, H. Xu, X.-W. Wang, Y.-X. Huang, M.B. Chan-Park, H. Zhang, L.-H. Wang, W. Huang, P. Chen, *ACS Nano* 6 (2012) 3206–3213.
- [18] S. Guo, S. Dong, E. Wang, *ACS Nano* 4 (2009) 547–555.
- [19] S. Bong, Y.-R. Kim, I. Kim, S. Woo, S. Uhm, J. Lee, H. Kim, *Electrochem. Commun.* 12 (2010) 129–131.
- [20] Y. Wang, Z. Shi, Y. Huang, Y. Ma, C. Wang, M. Chen, Y. Chen, *J. Phys. Chem. C* 113 (2009) 13103–13107.
- [21] C. Xu, X. Wang, J. Zhu, *J. Phys. Chem. C* 112 (2008) 19841–19845.
- [22] K. Zhang, Q. Yue, G. Chen, Y. Zhai, L. Wang, H. Wang, J. Zhao, J. Liu, J. Jia, H. Li, *J. Phys. Chem. C* 115 (2010) 379–389.
- [23] M.D. Stoller, S. Park, Y. Zhu, J. An, R.S. Ruoff, *Nano Lett.* 8 (2008) 3498–3502.
- [24] S. Park, Y. Shao, H. Wan, P.C. Rieke, V.V. Viswanathan, S.A. Towne, L.V. Saraf, J. Liu, Y. Lin, Y. Wang, *Electrochem. Commun.* 13 (2011) 258–261.
- [25] Y. Si, E.T. Samulski, *Chem. Mater.* 20 (2008) 6792–6797.
- [26] R.I. Jafri, T. Arockiadoss, N. Rajalakshmi, S. Ramaprabhu, *J. Electrochem. Soc.* 157 (2010) B874–B879.
- [27] Y. Li, Y. Li, E. Zhu, T. McLouth, C.Y. Chiu, X. Huang, Y. Huang, *J. Am. Chem. Soc.* 134 (2012) 12326–12329.
- [28] Y. Xin, J. Liu, X. Jie, W. Liu, F. Liu, Y. Yin, J. Gu, Z. Zou, *Electrochim. Acta* 60 (2012) 354–358.
- [29] A.L. Higginbotham, D.V. Kosynkin, A. Sinitskii, Z. Sun, J.M. Tour, *ACS Nano* 4 (2010) 2059–2069.
- [30] D.V. Kosynkin, A.L. Higginbotham, A. Sinitskii, J.R. Lomeda, A. Dimiev, B.K. Price, J.M. Tour, *Nature* 458 (2009) 872–876.
- [31] L.J. Cote, F. Kim, J. Huang, *J. Am. Chem. Soc.* 131 (2009) 1043–1049.
- [32] M.K. Debe, *Nature* 486 (2012) 43–51.
- [33] B.A. Kakade, T. Tamaki, H. Ohashi, T. Yamaguchi, *J. Phys. Chem. C* 116 (2012) 7464–7470.
- [34] B.A. Kakade, H. Wang, T. Tamaki, H. Ohashi, T. Yamaguchi, *RSC Adv.* 3 (2013) 10487–10496.
- [35] W. Li, C. Liang, W. Zhou, J. Qiu, H. Zhou, G. Sun, Q. Xin, *J. Phys. Chem. B* 107 (2003) 6292–6299.
- [36] Y. Mu, H. Liang, J. Hu, L. Jiang, L. Wan, *J. Phys. Chem. B* 109 (2005) 22212–22216.
- [37] W.X. Chen, J.Y. Lee, Z. Liu, *Chem. Commun.* 21 (2002) 2588–2589.
- [38] W.S. Hummers Jr., R.E. Offeman, *J. Am. Chem. Soc.* 80 (1958) 1339.
- [39] Y. Garsany, O.A. Baturina, K.E. Swider-Lyons, S.S. Kocha, *Anal. Chem.* 82 (2010) 6321–6328.
- [40] J.I. Paredes, S. Villar-Rodil, A. Martinez-Alonso, J.M.D. Tascon, *Langmuir* 24 (2008) 10560–10564.
- [41] D.C. Marcano, D.V. Kosynkin, J.M. Berlin, A. Sinitskii, Z. Sun, A. Slesarev, L.B. Alemany, W. Lu, J.M. Tour, *ACS Nano* 4 (2010) 4806–4814.
- [42] A.C. Ferrari, *Solid State Commun.* 143 (2007) 47–57.
- [43] W. Chen, L. Yan, P.R. Bangal, *Carbon* 48 (2010) 1146–1152.
- [44] W. Gao, L.B. Alemany, L. Ci, P.M. Ajayan, *Nat. Chem.* 1 (2009) 403–408.
- [45] Z. Fan, K. Wang, T. Wei, J. Yan, L. Song, B. Shao, *Carbon* 48 (2010) 1686–1689.
- [46] W. He, H. Jiang, Y. Zhou, S. Yang, X. Xue, Z. Zou, X. Zhang, D.L. Akins, H. Yang, *Carbon* 50 (2012) 265–274.
- [47] Q. Wu, Y. Xu, Z. Yao, A. Liu, G. Shi, *ACS Nano* 4 (2010) 1963–1970.
- [48] Y. Liang, H. Wang, J. Zhou, Y. Li, J. Wang, T. Regier, H. Dai, *J. Am. Chem. Soc.* 134 (2012) 3517–3523.
- [49] P. Kundu, C. Nethravathi, P.A. Deshpande, M. Rajamathi, G. Madras, N. Ravishanker, *Chem. Mater.* 23 (2011) 2772–2780.
- [50] A.R. Siamaki, A.E.R.S. Khder, V. Abdelsayed, M.S. El-Shall, B.F. Gupton, *J. Catal.* 279 (2011) 1–11.
- [51] Y. Xin, J. Liu, Y. Zhou, W. Liu, J. Gao, Y. Xie, Y. Yin, Z. Zou, *J. Power Sources* 196 (2011) 1012–1018.
- [52] C. Venkateswara Rao, C.R. Cabrera, Y. Ishikawa, *J. Phys. Chem. C* 115 (2011) 21963–21970.
- [53] J.D. Qiu, G.C. Wang, R.P. Liang, X.H. Xia, H.W. Yu, *J. Phys. Chem. C* 115 (2011) 15639–15645.

- [54] Y. Li, L. Tang, J. Li, *Electrochem. Commun.* 11 (2009) 846–849.
- [55] A. Kabbabi, R. Faure, R. Durand, B. Beden, F. Hahn, J.M. Leger, C. Lamy, *J. Electroanal. Chem.* 444 (1998) 41–53.
- [56] J. Lee, H. Ohashi, T. Ito, T. Yamaguchi, *J. Chem. Eng. Jpn.* 42 (2009) 918–929.
- [57] T. Nakajima, T. Tamaki, H. Ohashi, T. Yamaguchi, *J. Electrochem. Soc.* 160 (2013) F129–F134.